RSC Applied Interfaces

ROYAL SOCIETY OF CHEMISTRY

PAPER

View Article Online
View Journal

Cite this: DOI: 10.1039/d5lf00284b

Interface effects in molecular beam epitaxy of $SrMnSb_2$ on InAs and GaSb: segregation and endotaxy

Thomas J. Rehaag,[a] Ethan D. N. Dommett,[ab] Zhuo Yu,[a] Hong Yi Cheng Lin,[a] David Ironmonger,[a] Yisong Han[a] and Gavin R. Bell *[a]

Received 22nd September 2025,
Accepted 17th October 2025

DOI: 10.1039/d5lf00284b

rsc.li/RSCApplInter

Epitaxial growth of the topological semimetal $SrMnSb_2$ is demonstrated using InAs and GaSb substrates. The growth is studied by reflection high energy electron diffraction, X-ray photoemission spectroscopy and electron microscopy. The epitaxial orientation is $SrMnSb_2$ (001)||III–V (001), with the epilayer <010> axes parallel to substrate <110>. The relaxed in-plane lattice parameter of the epilayer depends on the vicinal miscut of the substrate and results in an overall volume expansion of the unit cell compared to bulk crystals, along with a possible lifting of the bulk orthorhombic distortion. Segregation of substrate atoms through the growing film is observed, along with Mn-driven endotaxial growth of secondary phases. Interface control methods to suppress endotaxial growth are discussed.

Open Access Article. Published on 17 October 2025. Downloaded on 10/27/2025 9:57:55 PM.
This article is licensed under a Creative Commons Attribution 3.0 Unported Licence.

1 Introduction

Semimetallic materials with topologically protected electronic states attract intense research effort because they show a range of new physical effects and could be exploited in novel electronic devices. The family $AMnPn_2$ (A = alkaline earth metal, Pn = pnictogen Sb or Bi) is of great interest[1] as a class of potential Dirac semimetals. For example, tuneable spin-valley coupling of Dirac nodes has been observed in $BaMnPn_2$.[2] Additional non-symmorphic crystal symmetries or magnetic order may induce Weyl physics. $SrMnSb_2$ is an antiferromagnetic semimetal which has been studied both theoretically and in bulk single crystal form.[1,3–10] A gapped Dirac dispersion is predicted at the *Y*-points of the Brillouin zone of $SrMnSb_2$, with a gap around 200 meV.[3,4] Remarkably, the material supports a coherent A_g phonon mode with frequency 4.4 THz which is predicted to narrow and, at sufficient amplitude, close the Dirac gap on femtosecond timescales 4. This offers unique possibilities for ultrafast control of Dirac and Weyl physics.[11]

Epitaxial thin film material is preferable to bulk single crystals for device applications: not only does it allow efficient device processing and improved compatibility with existing electronic materials, but additional control is possible *via* quantum size effects, strain engineering and magnetic proximity effects. Crucially, the effects of the coherent phonon could be studied by ultra-fast pump-probe spectroscopy of thin-film $SrMnSb_2$.[11] Although the related materials SrMnBi2 (ref. 12 and 13) and MnSb (ref. 14) have been grown using molecular beam epitaxy (MBE), thin-film $SrMnSb_2$ has not yet been grown and characterised. The MBE growth of transition metal pnictides such as MnSb,[15–18] CrSb (ref. 19) and NiSb (ref. 20) is quite well established.[21] In many respects the surface chemistry of the epitaxy appears to follow that of the III–V semiconductors, at least in respect of the pnictogen. At sufficiently high substrate temperature, incorporation of the group V element is self-limiting, leading to stoichiometry between the transition metal and pnictogen components. At too low a substrate temperature, excess pnictogen may be incorporated. Excessively high substrate temperature leads to the group V element re-evaporating before incorporation.[18] However, the growth window between these two extremes is wide (at least 200 °C for MnSb) and so there is scope for MBE optimisation on different substrates. Endotaxial growth of secondary phases has been noted for MnSb grown on both GaSb (ref. 22) and InP, (ref. 23) and for MnP on GaP,[24] *i.e.* these phases form as nano-crystals *below* the initial substrate surface. This is potentially

[a] *Department of Physics, University of Warwick, Coventry CV4 7AL, UK. E-mail: gavin.bell@warwick.ac.uk*
[b] *CY Cergy Paris University, Boulevard du Port 95011, Cergy-Pontoise, France*

© 2025 The Author(s). Published by the Royal Society of Chemistry

problematic for $SrMnSb_2$, whose antiferromagnetism may be masked by ferromagnetic secondary phases such as MnSb or MnAs.

In this paper we describe the MBE growth of $SrMnSb_2$(001) on InAs and GaSb(001) substrates. The primary interfacial effects of segregation and endotaxy are explored using structural and chemical analysis.

2 Crystal structure and heteroepitaxy

Our choice of InAs and GaSb as substrates was motivated by minimisation of epitaxial strain and symmetry mismatch. The $SrMnSb_2$ lattice structure is illustrated[25] in Fig. 1. The orthorhombic unit cell[7] (shown as the rectangular frame in the figure) has c much larger than a or b, which are not quite equal. Note that we choose to denote the long axis as c so that [001] is the epitaxial growth direction; the space group of bulk $SrMnSb_2$ is then *Pcnm*.[1] The bulk unit cell dimensions were measured as (4.41, 4.46, 23.10) Å for recent stoichiometric bulk material.[10] The [001] layering arrangement can be described as $MnSb_4$ tetrahedra separated by checkerboard pattern Sr–Sb in sandwich structures. Mn and Sr atoms share no bonds with each other and are separated by intermediate Sb planes. The Sr–Sb arrangement is slightly different in each $c/2$ half of the unit cell, which is also observed in $SrZnSb_2$.[5,26] The Sb(1) layer differs from structures such as the equivalent Bi(1) layer of $SrMnBi_2$ by

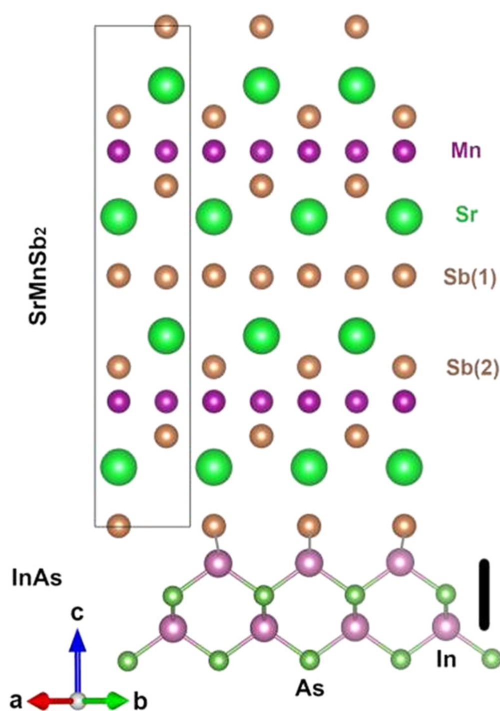

Fig. 1 $SrMnSb_2$ crystal structure and possible epitaxy on InAs(001). The crystallographic axes refer to the substrate and colour-coded atoms are labelled in the figure. The $SrMnSb_2$ is shown in the ac-plane and the InAs in a [110] plane. The vertical black bar represents the surface atomic step height on InAs(001).

a subtle distortion in the otherwise 2D square lattice,[27] incurred *via* a Peierls distortion,[28] and results in a buckled atom arrangement with orthorhombic symmetry. Under external stress, the unit cell structure can instead maintain a square Sb(1) lattice *via* the same mechanism as $SrMnBi_2$, in which the strong spin–orbit coupling (SOC) suppresses the distortion. The weaker SOC in Sb interactions can overcome the buckling phenomenon by inducing a compression of the total cell volume by 10%, forcing the interatomic distances to contract and thus flattening the Sb layer and closing the band gap.[3] It is plausible that epitaxial strain could also affect the orthorhombic distortion.

Fig. 1 shows a possible epitaxial arrangement on InAs(001). The (a, c) axes of the $SrMnSb_2$ align with the [110] and [1̄10] primitive surface mesh axes of the InAs with average lattice mismatch 3.2%. This is indeed the observed epitaxial relationship, although the precise interfacial atomic structure is not known. The figure illustrates the lower Sb(1) layer of the $SrMnSb_2$ adopting the approximate atomic positions of the surface As atoms in bulk-like As-terminated InAs(001). The vertical black bar represents the $a/2 \approx 3$ Å step height on InAs(001), which is far smaller than the c lattice parameter of $SrMnSb_2$. Short grey lines joining In to Sb atoms represent interfacial bonds with an exaggerated in-plane epitaxial mismatch.

Epitaxial mismatches (% change between film and substrate lattice parameter, normalised to the latter) are shown in Table 1 for several common semiconductor materials. Negative values indicate that the $SrMnSb_2$ must be compressively strained to match the substrate, and the positive values (for InSb only) would require tensile strain in the $SrMnSb_2$. The (a, b) column uses the averaged in-plane lattice paramter of $SrMnSb_2$ and this quanitity will be discussed subsequently. A good lattice match to the average (a, b) spacing of bulk $SrMnSb_2$ could be achieved by growing on the ternary materials $InAs_{0.5}Sb_{0.5}$ or $Ga_{0.6}In_{0.4}Sb$.

The critical thickness d_c for plastic relaxation *via* misfit dislocations is also tabulated. This was estimated using the People-Bean model[29] evaluated in closed form using the Lambert W-function.[30] Elastic constants are taken from first-principles calculations reported in Materials Project.[31] Because the Burgers vectors of misfit dislocations in $SrMnSb_2$ are not known, a range from $a\sqrt{2}$ to a is used. The three high-mismatch substrates are out of the range of validity of the continuum elastic model. The calculation suggests that pseudomorphic $SrMnSb_2$ should be observable on GaSb(001),

Table 1 Epitaxial mismatch and critical thickness d_c for $SrMnSb_2$

Substrate	% (a)	% (b)	% (a, b)	d_c (nm)
InAs	−2.6	−3.7	−3.2	4.8–11.4
GaSb	−2.0	−3.1	−2.5	9.9–22.5
InSb	4.1	3.0	3.5	3.6–8.7
GaAs	−9.9	−11.1	−10.5	
Si	−14.5	−15.7	−15.1	
$SrTiO_3$	−12.9	−14.2	−13.6	

Open Access Article. Published on 17 October 2025. Downloaded on 10/27/2025 9:57:55 PM.
This article is licensed under a Creative Commons Attribution 3.0 Unported Licence.

© 2025 The Author(s). Published by the Royal Society of Chemistry

Open Access Article. Published on 17 October 2025. Downloaded on 10/27/2025 9:57:55 PM.
This article is licensed under a Creative Commons Attribution 3.0 Unported Licence.

but that relaxation may occur on InAs(001) before even 2 ML film thickness (here defining 1 monolayer, ML, of $SrMnSb_2$ as one bulk unit cell, 2.3 nm height).

3 Experimental methods

The two readily available low-mismatch substrates, InAs and GaSb, were used, with and without GaSb buffer layers. Miscut (vicinal) substrates are often used in MBE to promote layer-by-layer growth or suppress anti-phase boundaries, and several vicinal miscuts of InAs(001) were also investigated. Substrate wafers were cleaved to roughly 8 mm square pieces and mounted to sample transfer flags using spot-welded Ta strips. Preparation of clean, reconstructed, III-terminated surfaces was achieved by a combination of chemical cleaning (dip in HCl : isopropanol mix) immediately before loading to vacuum under dry nitrogen, argon ion sputtering (500 eV ion energy, 1 μA beam current) and annealing. The types of substrate and buffer layer are summarised in Table 2. For all substrates, $SrMnSb_2$ growth was performed either directly on the cleaned substrate or on a GaSb buffer layer.

The MBE growth was performed using shuttered effusion cells for Ga, Sr, Mn and Sb_4. These were calibrated using beam equivalent pressure (BEP) from a retractable ion gauge, and *via* scanning transmission electron microscopy (STEM) measurements of total film thicknesses. Growth was monitored using reflection high energy electron diffraction (RHEED) with a 12.5 keV beam. The fluxes and substrate temperature were initially based on our experience with MBE growth of MnSb,[17,32] treating the summed Sr and Mn fluxes as equivalent to the Mn flux for MnSb. Optimising the quality of the RHEED patterns from this starting point led to the following standard growth conditions: substrate temperature T_{sub} = 340 °C, BEP ratios Sr : Mn : Sb approximately 1.0 : 1.2 : 6.5, total growth rate 0.6 nm min^{-1}, film thickness between 12 and 120 nm (5 to 50 ML). Any variations on these conditions are discussed in the individual results sections. The GaSb(001) buffer layers were grown at T_{sub} = 360 °C and 0.7 nm min^{-1}.

The STEM experiments were performed in a double aberration-corrected JEOL ARM200f TEM, operated at 200 kV. This TEM is equipped with an Oxford Instruments SDD energy dispersive X-ray analysis (EDX) detector, and elemental maps were obtained for the main elements in the heterostructures. Additional standard TEM images were obtained using a JEOL 2100 microscope, also operating at 200 kv. Samples were transferred either through air or *via* vacuum suitcase to separate chambers for study by X-ray photoelectron spectroscopy (XPS). X-ray diffraction (XRD) was also performed on selected films (Panalytical X'Pert Pro MRD, Cu Kα radiation). Samples transferred by air were protected from oxidation by arsenic caps deposited in a side chamber on the MBE vacuum system. Some samples were also capped with Sb by cooling in the MBE chamber under Sb_4 flux. Caps were not completely removed in XPS since the maximum annealing temperature used was set at the MBE substrate temperature.

Table 2 Substrate types for $SrMnSb_2$ heteroepitaxy

Material	Miscut (°)	Buffer (nm)	Section
InAs	0 ± 0.1, 0.5, 1, 2	None	4.1, 4.2
InAs	0 ± 0.1, 0.5, 1, 2	GaSb 10–20 nm	4.1, 4.4
GaSb	0 ± 0.1	None	4.1, 4.3
GaSb	0 ± 0.1	GaSb 10–20 nm	SI

4 Results and discussion

4.1 General results

Before discussing the individual interfaces, we show a selection of results to highlight common features. Fig. 2 shows RHEED patterns for $SrMnSb_2$ grown on a GaSb(001) buffer layer on InAs(001). Row (a) shows the initial InAs surface, which displays a (4 × 2) periodicity as expected for an In-stable surface prepared without As flux. Strong Kikuchi features characteristic of the zincblende B3 structure are visible. Row (b) shows the GaSb buffer layer surface (20 nm grown) with (1 × 3) surface periodicity. The GaSb is pseudomorphic to the InAs substrate and the Kikuchi features are identical. Row (c) shows the $SrMnSb_2$ surface (12 nm or 5 ML grown). The in-plane lattice parameters have relaxed to larger values, slightly larger than the bulk (a, b) lattice parameters of $SrMnSb_2$. The Kikuchi features have vanished and there is no surface reconstruction. The RHEED pattern is streaky but the background is higher and some modulation and spots are visible on the streaks. In general, the background intensity and spottiness of the RHEED

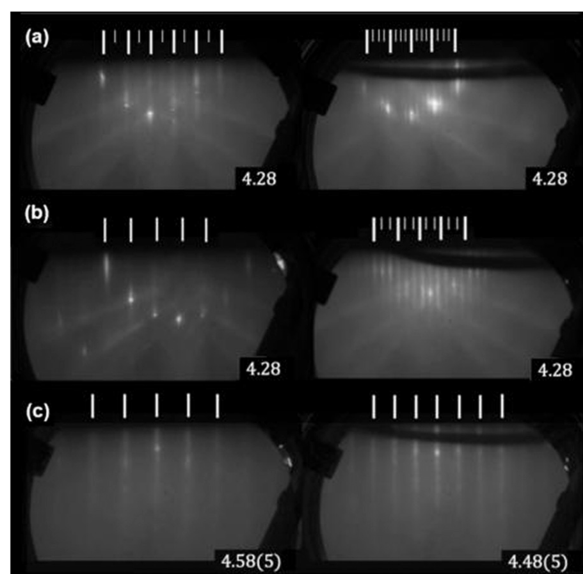

Fig. 2 RHEED patterns for $SrMnSb_2$ grown on GaSb buffer on InAs(001) in the [110] and [110] azimuths. Long white dashes indicate integer order surface streaks, while short dashes highlight fractional orders. Inset numbers show the lattice parameter in Å. Row (a) shows the as-prepared InAs(001) surface. Row (b) shows the completed GaSb(001) buffer layer. Row (c) shows the completed $SrMnSb_2$ layer.

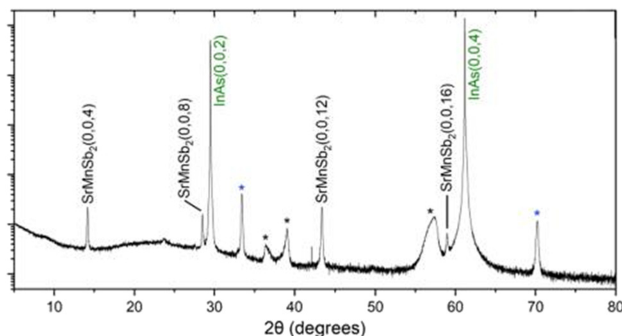

Fig. 3 XRD data for 80 nm $SrMnSb_2$ grown directly on InAs(001). Substrate and $SrMnSb_2$ peaks are labelled. The asterisks denote secondary phases.

patterns increased at higher $SrMnSb_2$ film thicknesses. It was not possible to distinguish between the *a* and *b* lattice parameters in RHEED, although the precision of the relative lattice parameter measurement should be sufficient (SI). For all $SrMnSb_2$ films studied, the streak spacings in orthogonal the [10] and [01] directions were identical within the measurement uncertainty. This is compatible with tetragonal rather than orthorhombic symmetry.

Fig. 3 shows XRD data for a thick $SrMnSb_2$ epilayer grown directly on InAs(001). Apart from the substrate peaks, a family of sharp peaks is visible which can be assigned to $SrMnSb_2(0004n)$ reflections. Together with the RHEED data, this confirms the epitaxial orientation of $SrMnSb_2$. The peak series can be fitted with a lattice parameter of 25.074(4) Å, slightly larger than the *c* parameter of bulk crystals.[10] Scherrer analysis (SI) gives a crystallite size of 10.7 nm, significantly smaller than the film thickness. This indicates that the epilayer contains domains or other extended defects, consistent with the poorer RHEED patterns for the thickest films. The XRD peaks labelled with asterisks correspond to secondary phases. The blue asterisk peaks (5.37 Å) can be tentatively identified with strained orthorhombic MnAs.[21,32] The remaining peaks, black asterisks, can be tentatively assigned to cubic MnSb (ref. 32) and InSb. Note that if the unit cell of the $SrMnSb_2$ epilayer is identified as tetragonal rather than orthorhombic, then the main peaks can be assigned to $(0002n)$ reflections with $c = 12.537(4)$ Å.

Fig. 4 shows example STEM and EDX data. Panel (a) gives an annular dark field (ADF) STEM image of a well ordered region of a $SrMnSb_2$ film, which was grown on an InAs(001) substrate miscut by 1° towards (111)B. The orthorhombic bulk unit cell is outlined by an orange box (4.6 Å × 24.1 Å). Panels (b, c, d, e) show a STEM image and the corresponding EDX elemental maps, obtained from a $SrMnSb_2$ sample grown directly on InAs(001). The $SrMnSb_2$ epilayer is less uniform and its interface to InAs, appearing as a dark horizontal band, is rougher. Furthermore, a triangular or dome-like feature is visible below the substrate surface. As shown by the elemental maps, Sr and Mn appear in the epilayer, as expected. However, the Mn signal follows the shape of the dome-like sub-surface feature. The As signal of

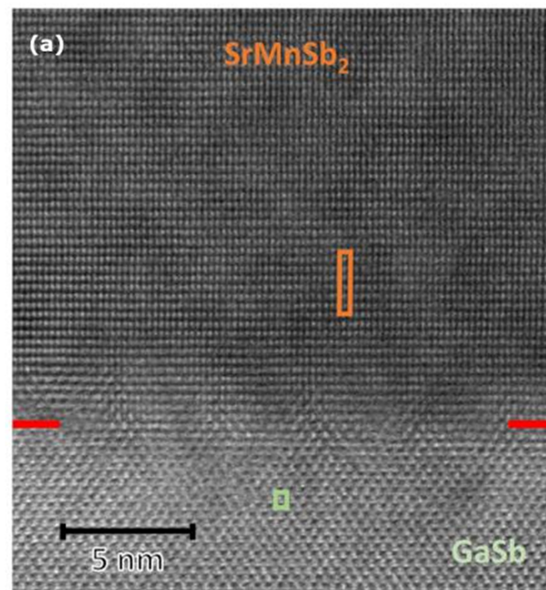

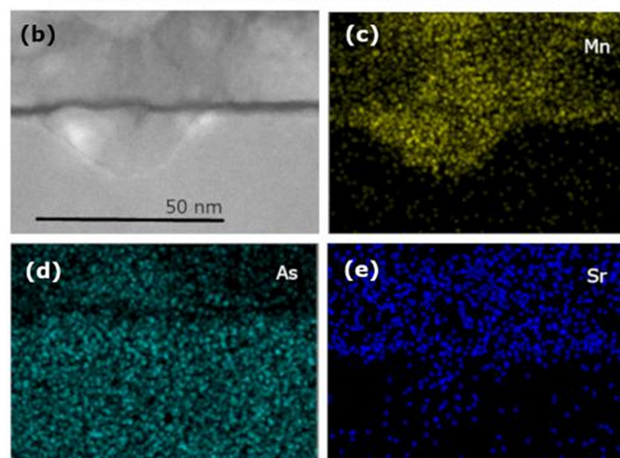

Fig. 4 Example STEM-EDX data. (a) ADF STEM image for $SrMnSb_2$ grown directly on GaSb(001), with interface highlighted by red dashes. The bulk unit cells of GaSb and $SrMnSb_2$ are highlighted by coloured boxes. Panel (b) shows a BF STEM image of a sample grown directly on InAs(001). The interface appears as a dark band and a triangular feature is visible below the substrate surface. EDX data are shown for Mn, As and Sr in panels (c), (d) and (e) respectively, identifying this feature as endotaxial MnAs.

the InAs substrate is quite uniform, allowing us to identify the subsurface nano-cluster as endotaxial MnAs. A small amount of Sr also appears in the endotaxial nano-cluster. Finally, a significant As signal [panel (c)] is observed in the $SrMnSb_2$ epilayer above the endotaxial cluster, indicating local segregation of As from the substrate into the growing film.

Fig. 5 gives XPS data for films grown directly on InAs and GaSb substrates. Panel (a) shows an XPS survey scan after vacuum suitcase transfer of a 35 nm thick film. No O 1s or C 1s peaks can be observed, indicating that the suitcase transfer did not introduce any surface contamination. The films have complete coverage and are sufficiently thick to prevent photoelectrons escaping from the substrate, and so

Open Access Article. Published on 17 October 2025. Downloaded on 10/27/2025 9:57:55 PM.
This article is licensed under a Creative Commons Attribution 3.0 Unported Licence.

© 2025 The Author(s). Published by the Royal Society of Chemistry

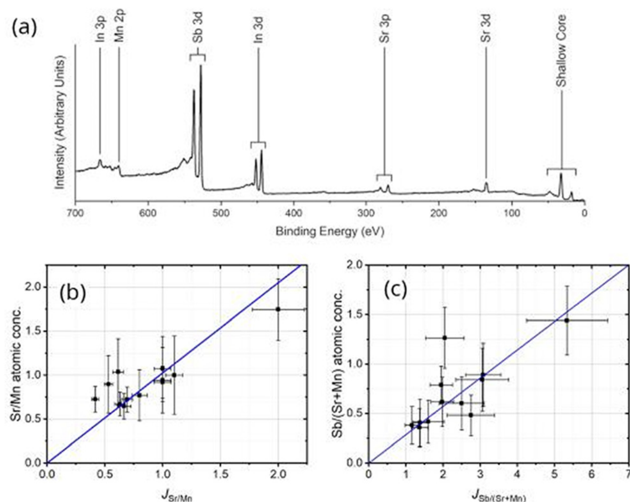

Fig. 5 (a) XPS survey scan for a $SrMnSb_2$ sample grown directly on InAs(001), with all peaks indexed. (b) Sr/Mn composition ratio inferred from XPS as a function of Sr/Mn BEP ratio. (b) Sb/(Sr + Mn) composition ratio inferred from XPS as a function of Sb/(Sr + Mn) BEP ratio. In (b) and (c) the blue straight lines indicate stoichiometric incorporation.

the presence of clear In 3d and 3p peaks implies that In has segregated through the $SrMnSb_2$ film.

The XPS was quantified using standard atomic sensitivity factors, with results for [Sr]/[Mn] ratios and [Sb]/([Sr] + [Mn]) ratios shown in Fig. 5(b) and (c) respectively. The [Sr]/[Mn] ratio inferred from XPS follows stoichiometric incorporation of the fluxes as measured by BEP, with a slight excess of Sr possible at low BEP ratio. The Sb incorporation shows a similar trend with BEP ratio. Although the Sb incorporation does not seem to show clear self-limiting behaviour, as is the case for MnSb,[21] only two data points lie above the line [Sb]/([Sr] + [Mn]) = 1. The BEP standard ratios used aim to provide stoichiometric $SrMnSb_2$ and the average Sr : Mn : Sb atomic ratios inferred from XPS for samples grown close to the standard conditions were 1 : 0.89 : 1.95.

To summarise these general results, the RHEED and XRD confirm that the epitaxial orientation of the $SrMnSb_2$ has the long [001] axis out of plane and the [100] and [010] axes aligned with substrate [110] and [110] bulk axes (*i.e.* the primitive surface mesh [10] and [01] axes). Diffraction results are compatible with relaxation of the orthorhombic distortion of bulk material towards a smaller tetragonal unit cell. The standard growth conditions produce $SrMnSb_2$ films with close to stoichiometric composition. For growth on InAs substrates, indium surface-segregates through the films. Furthermore, endotaxial growth of MnAs nano-clusters within the substrate occurs, accompanied by some local diffusion of As into the epilayer and Sb-related secondary phases.

4.2 Direct growth on InAs(001)

Fig. 6 shows a sequence of RHEED patterns for direct deposition of $SrMnSb_2$ on InAs(001) [T_{sub} = 360 °C]. The as-prepared InAs surface shows the expected (4 × 2) or c(8 × 2) periodicity, with half-order streaks clearly present in the [110] RHEED pattern [Fig. 6(a)]. These fractional order streaks vanish almost immediately when $SrMnSb_2$ growth is initiated by opening all three shutters simultaneously. Panel (b) shows only integer order streaks after just 0.25 ML $SrMnSb_2$ coverage (0.6 nm). This is also true for the [110] azimuth; indeed, throughout the experiments no surface reconstruction of $SrMnSb_2$ was observed, *i.e.* (1 × 1) periodicity only. As growth proceeds, modulation appears along the diffraction streaks, which evolves into a mixed spotty/streaky pattern (c, d). This indicates increasing roughness leading to transmission diffraction. The spots lie on the surface streaks which indicates that the material growing as 3D islands is the same as that growing in layer-by-layer fashion, and is co-epitaxial.

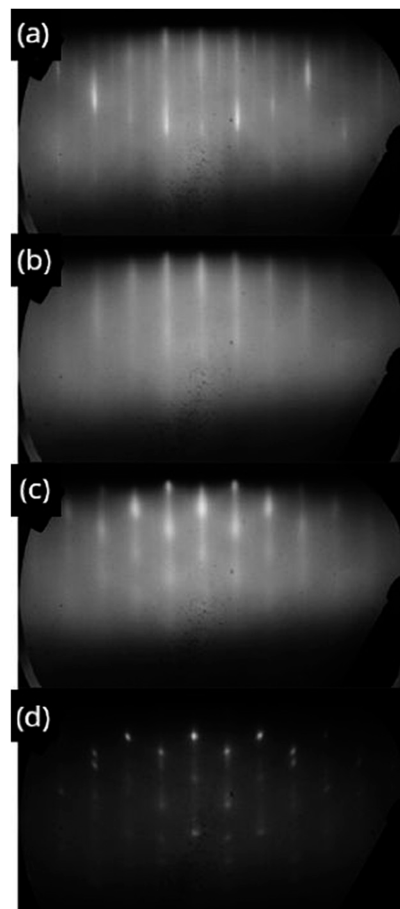

Fig. 6 RHEED patterns in the [110] direction for $SrMnSb_2$ grown directly on InAs(001). (a) As-prepared InAs(001) surface, with 2× periodicity; (b) 1 minute $SrMnSb_2$ deposited (0.6 nm ≈ 0.25 ML); (c) 4 nm deposited; (d) 50 nm desposited.

The in-plane lattice parameter measured by RHEED rapidly increases from the substrate value as growth proceeds, as shown in Fig. 7 for two different substrate miscuts. At the earliest stages of growth, up to 1 ML $SrMnSb_2$ coverage, the lattice parameter remains at the

Open Access Article. Published on 17 October 2025. Downloaded on 10/27/2025 9:57:55 PM.
This article is licensed under a Creative Commons Attribution 3.0 Unported Licence.

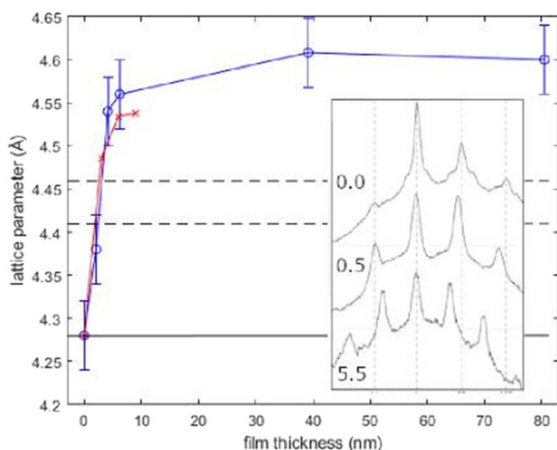

Fig. 7 In-plane lattice parameter as a function of film thickness, as inferred from streak spacings in RHEED. The InAs in-plane lattice parameter is highlighted by the solid horizontal line, while the dashed lines shown bulk (a, b) parameters for $SrMnSb_2$. Blue open circles correspond to $SrMnSb_2$ directly grown on InAs(001) miscut by 2°, while red crosses shown a sample miscut by 1°. Inset are typical RHEED intensity profiles for 0, 0.5 and 5.5 ML $SrMnSb_2$ growth. Vertical dashed lines on the inset represent substrate streak spacing.

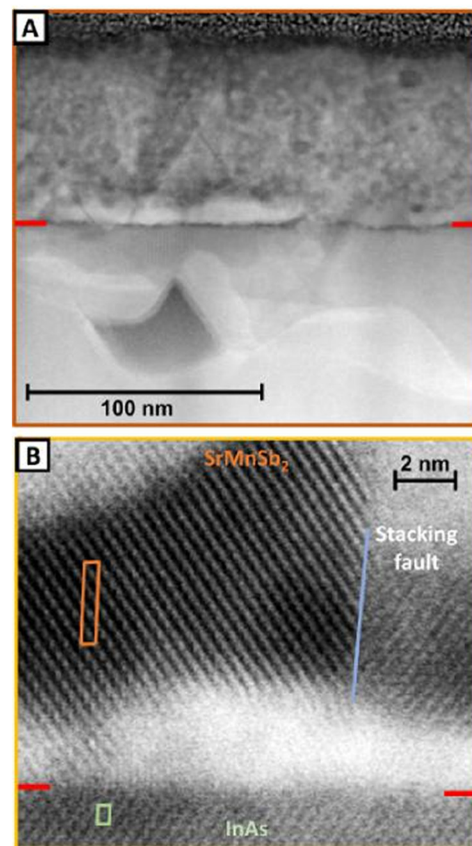

Fig. 8 TEM and STEM images for $SrMnSb_2$ grown directly on InAs(001), with interface highlighted by red dashes. The large scale image A shows some disruption at and below the interface (red dashes), and grain structure in the film. Image B at high magnification shows the unit cells of film and substrate (orange and green rectangles). A stacking fault is highlighted by a blue line.

substrate value (SI). Full relaxation occurs by around 5 to 10 ML coverage (10 to 20 nm). These values are broadly in line with the estimated critical thicknesses (Table 1). However, the lattice parameter clearly increases *past* the nominal bulk values. The "over-relaxation" is unusual, especially when considered alongside the out-of-plane lattice expansion relative to bulk material inferred from XRD (Fig. 3). Combining the two expansions, the unit cell volume of the epitaxial material ($4.6 \times 4.6 \times 25.074$ Å^3) is increased by 16% compared to the bulk crystal ($4.41 \times 4.46 \times 23.1$ Å^3).[10] This is not compatible with a biaxial distortion from the substrate mismatch. The different strain relaxation for growth on two different InAs(001) miscuts is suggestive of strain relaxation *via* vicinal surface epitaxy, as previously observed for III-nitride growth on SiC,[33,34] Ga_2O_3 on sapphire[35] and chalco-genide films on Si.[36]

When the RHEED patterns become spotty, it is possible to measure the out-of-plane lattice parameter of the film (SI). These measurements give values close to $c/2$. This agrees with the X-ray diffractogram (Fig. 3), which shows the (0 0 4n) family of peaks (n = 1, 2, …) rather than the (0 0 2n). This can be interpreted as a lifting of the distortions which distinguish the two halves of the full c = 23.10 Å unit cell and split the (a, b) lattice parameters, and is consistent with observation by RHEED of equal (a, b) values. This smaller tetragonal unit cell is very close in energy (1 meV per atom (SI)) to the orthorhombic ground state[31] and could readily be stabilised by epitaxial strain or the presence of segregated substrate atoms in the structure.

The crystallite size was inferred from XRD as being smaller than film thickness, and this is confirmed by TEM. Fig. 8 shows example images from $SrMnSb_2$ grown directly on InAs(001). Image A shows a region of crystallographic disruption at the interface and grain-like structures above in the film. There is also clear endotaxial disruption below the interface. Atomic scale imaging is shown in B, with unit cells highlighted. The TEM data supports the epitaxial relationship and lattice parameters inferred from RHEED and XRD. However, a clear grain boundary is visible, most likely associated with a stacking fault. There is also a significant loss of atomic scale contrast close to the interface. The effective gain size is inevitably less than the film thickness for such samples. Smaller and more crystallographically diverse grains are observed in films with poorer RHEED patterns and a higher degree of endotaxial disruption (SI).

Three methods to suppress the endotaxial growth were investigated: (1) low temperature seed layer, (2) Sb soak, and (3) Sr–Sb growth initiation (delayed Mn flux). For (1), the substrate temperature was reduced to the range 30 °C to 200 °C for initial $SrMnSb_2$ growth up to a few ML thickness. However, this resulted in rapid and unrecoverable degradation of the RHEED pattern and was abandoned. For the Sb soak (2), the InAs(001) surface was

Open Access Article. Published on 17 October 2025. Downloaded on 10/27/2025 9:57:55 PM. This article is licensed under a Creative Commons Attribution 3.0 Unported Licence.

 © 2025 The Author(s). Published by the Royal Society of Chemistry

exposed to Sb flux for several minutes at the standard substrate temperature prior to initiation of $SrMnSb_2$ growth. The intention was to allow any excess In atoms at the surface to react with Sb and hence suppress surface segregation of In. This procedure caused the fractional order RHEED streak intensity of the initial (4 × 2) to be reduced but did not degrade the RHEED pattern of the subsequent $SrMnSb_2$ epilayers. However, segregated In was still observed in XPS, suggesting that the out-diffusion of In is not just a consequence of In nano-clusters or adatoms left from the surface cleaning process.[37] For procedure (3), the Sr shutter was opened 30 s before the Mn shutter (since the predominant endotaxial species was MnAs, it was hoped to discourage direct Mn interaction with the substrate). The $SrMnSb_2$ RHEED patterns were marginally better, and TEM data suggest that there is an overall reduction in secondary phase formation (SI). In addition, the delayed Mn flux reduced the concentration of surface-segregated indium by around 20%, according to XPS, and so this simple procedure was retained.

Clearly, the endotaxial growth of MnAs and related phases, along with concomitant segregation of In and As into the epilayer, has a deleterious effect on the uniformity of the $SrMnSb_2$ and the quality of the interface. Furthermore, MnAs is ferromagnetic[21] and could easily mask the desired antiferromagnetic response of the $SrMnSb_2$. We therefore consider GaSb substrates.

Open Access Article. Published on 17 October 2025. Downloaded on 10/27/2025 9:57:55 PM.
This article is licensed under a Creative Commons Attribution 3.0 Unported Licence.

4.3 Direct growth on GaSb(001)

GaSb offers the lowest lattice mismatch (Table 1) as well as avoiding any problems arising from As segregation into the $SrMnSb_2$. For direct growth on the as-prepared GaSb(001) substrates, an Sb soak was used to improve the initial GaSb(001) surface reconstruction and the delayed Mn flux protocol was employed. The evolution of RHEED patterns was very similar to that observed on buffer layers (Fig. 2) though with slightly worse quality and a higher tendency to show transmission diffraction spots. Despite this, the interface quality was generally improved over growth on InAs(001). Fig. 4(a) shows a STEM image of the $SrMnSb_2$/GaSb interface at high resolution. While not atomically abrupt, the interface is reasonably sharp, transitioning between structures within a few unit cells either side of the nominal interface. There is no evidence of dislocations or other extended defects in this region of the film.

However, some segregation and endotaxial growth were observed. Fig. 9 shows a STEM image and selected (SI) EDX elemental maps for a $SrMnSb_2$/GaSb(001) interface. On this wider view, the interface is still quite abrupt but some evidence for endotaxial growth and segregation. Two dome-like protrusions of Mn some tens of nm into the substrate can be seen in the centre of the Mn EDX map. The corresponding Sb map is quite uniform, suggesting that a MnSb phase has formed. There is a noticeable Ga deficiency close to the interface above the right hand side MnSb endotaxial nano-cluster, and above that a sharp "streak" of Ga can be seen within the $SrMnSb_2$ film. This shows that local Ga segregation has occurred. Sb is deficient on this streak, and there is a slight excess of Mn. The surface of the $SrMnSb_2$ film is defined by the Mn and Sb EDX maps. It is not planar but rather comprises mesa-like structures with flat tops. This morphology is consistent with the spotty RHEED patterns observed at higher film thicknesses.

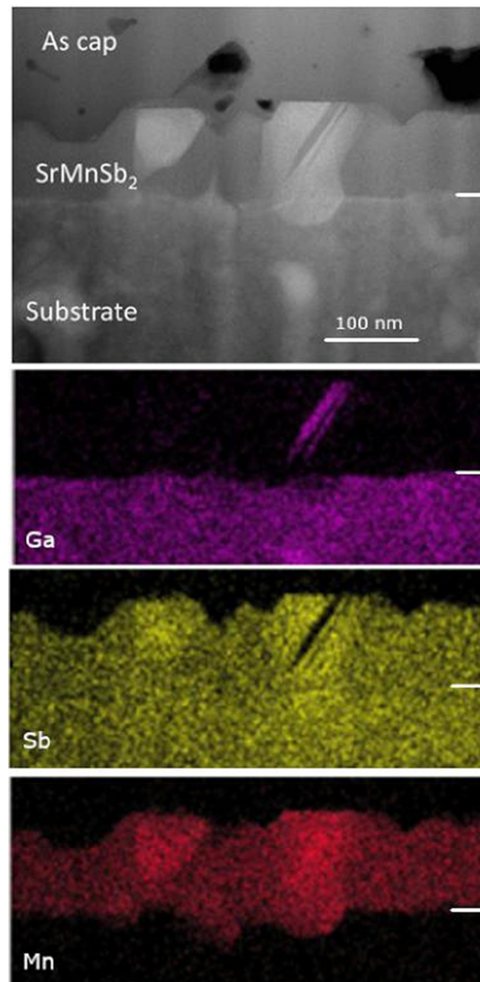

Fig. 9 STEM image and three EDX maps (Ga, Sb, Mn) for $SrMnSb_2$ grown directly on GaSb(001). The interface is highlighted by white dashes on the right in each panel.

The over-relaxation of the $SrMnSb_2$ epilayer also occurs on this substrate. Estimating unit cell dimensions from STEM (Fig. 4) gives a volume of (4.6 × 4.6 × 24.1 $Å^3$), a volume expansion of 12% compared to bulk material.

4.4 Growth on GaSb buffer layers

GaSb(001) buffer layers were grown on both InAs(001) and GaSb(001) substrates. These were thin (10 to 20 nm) and were pseudomorphic on InAs(001) as expected. Typical

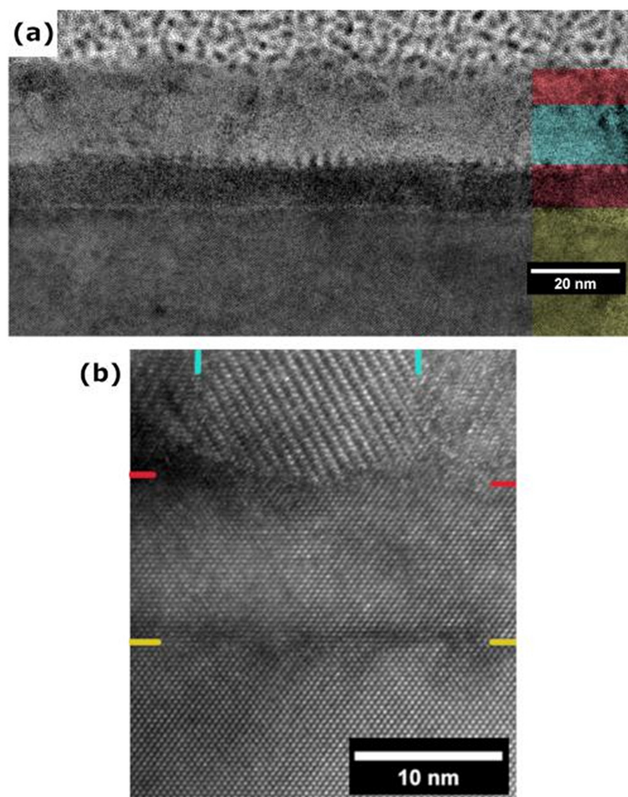

Fig. 10 TEM images of a $SrMnSb_2$ sample grown on a GaSb buffer layer on InAs(001). Panel (a) shows an overview with colour blocks on the right highlighting the layer structure (yellow InAs, red GaSb, teal $SrMnSb_2$). Panel (b) shows a higher resolution image of the GaSb buffer layer interfaces to the underlying InAs (yellow dashes) and the overgrown $SrMnSb_2$ (red dashes). Vertical teal dashes show two grain boundaries in the $SrMnSb_2$ epilayer.

Open Access Article. Published on 17 October 2025. Downloaded on 10/27/2025 9:57:55 PM. This article is licensed under a Creative Commons Attribution 3.0 Unported Licence.

RHEED results were already shown in Fig. 2 for a sample grown using standard conditions. In such conditions, the $SrMnSb_2$ RHEED patterns were less spotty on GaSb buffer layers than when grown directly on as-prepared GaSb(001). This is in line with the results on InAs(001), where a poorer starting surface led to poor and unrecoverable $SrMnSb_2$ RHEED. Indium segregation is expected for the GaSb-on-InAs interface[38–40] and segregated In was observed in XPS for these buffer layers (SI).

Two TEM images of a sample grown on 15 nm GaSb–InAs(001) buffer layer are shown in Fig. 10. In panel (a), the InAs-to-GaSb interface appears as a lighter band, with the GaSb buffer layer darker than the substrate (colour highlights on the right guide the eye). The interface between the GaSb buffer and the $SrMnSb_2$ is not atomically abrupt. However, there is no evidence for significant endotaxial phase formation. Available measurements over several samples suggest that endotaxial growth was significantly less prevalent for samples growth on buffer layers compared to direct growth on GaSb. Note that this sample was capped with a thin GaSb layer, which shows a granular structure (top layer highlighted in red). Panel (b) shows a higher magnification image of the interfaces. Yellow dashes highlight the abrupt GaSb-on-InAs interface, with the GaSb showing a continuous pseudomorphic crystal structure. The red dashes show the $SrMnSb_2$-on-GaSb interface, which is less abrupt and fluctuates by several atomic layers. The $SrMnSb_2$ film shows three domains. The TEM images and RHEED (Fig. 2) confirm the improved $SrMnSb_2$ film quality when grown on GaSb buffer layers, even when they are thin (as low as 10 nm).

Conclusions

Thin epitaxial films of $SrMnSb_2$(001) have been grown on GaSb(001) and InAs(001) substrates. The in-plane epitaxial orientation has epilayer <010> axes parallel to substrate <110>. The in-plane strain is relaxed rapidly, with only around 1 ML of pseudomorphic growth. Films typically "over-relax", with unit cell volume expansion up to 16% above the nominal bulk values, and the overall relaxation is affected by the vicinal miscut of the substrate. In diffraction, $(0004n)$ peaks are observed and the (a, b) lattice parameters cannot be distinguished. This is compatible with the orthorhombic distortion present in bulk crystals being lifted in epilayers, which could adopt a tetragonal structure with c lattice parameter around half the bulk value. Further study of the crystal structure of the epilayers using synchrotron XRD would be valuable.

Growth is hampered by the formation of endotaxial secondary phases alongside segregation of atoms from the substrate. This is particularly severe for direct growth on InAs substrates, where MnAs nanoclusters and other phases are formed. Both In and As segregate into the $SrMnSb_2$ films, the former surface-segregating through the films to give a prominent In signal in XPS. Arsenic segregation appears to associated more with local defect phases, as does Ga segregation for growth on GaSb. Controlled interface formation by Sb soak and delayed Mn exposure helped to limit endotaxial phase formation. Overall, in order of prevalence of endotaxial growth, direct growth on InAs substrates was worst, followed by direct growth on GaSb, with growth on GaSb buffer layers the most favourable.

A promising method for reliably suppressing endotaxial growth is remote epitaxy *via* the inclusion of an ultra-thin amorphous carbon layer.[41] This acts to decouple the growing film from the substrate while maintaining the epitaxial relationship. A key advantage of amorphous carbon is that it can be grown *in situ* on any III–V substrate and does not require wet or dry transfer, as would be the case for a 2D material such as graphene. To our knowledge, this application of remote epitaxy has not yet been studied. A longer Sb soak for interface optimisation of GaSb buffer layers[39] may also improve the surface quality for $SrMnSb_2$ epitaxy. Atomic exchange models with multiple species,[38] extended to include Mn, may be useful in understanding endotaxial growth.

 © 2025 The Author(s). Published by the Royal Society of Chemistry

Open Access Article. Published on 17 October 2025. Downloaded on 10/27/2025 9:57:55 PM.
This article is licensed under a Creative Commons Attribution 3.0 Unported Licence.

Author contributions

Bell, Rehaag: conceptualization, writing – original draft, formal analysis, methodology. Bell: supervision. All authors: investigation, writing – review & editing.

Conflicts of interest

There are no conflicts to declare.

Data availability

Data for this article, including RHEED and TEM, are available at Warwick Research Archive Portal at **https://wrap.warwick.ac.uk/192906**.

Supplementary information: this includes additional analysis of RHEED, XRD, TEM and XPS. See DOI: **https://doi.org/10.1039/d5lf00284b**.

Acknowledgements

The authors are grateful to Dr. David Walker for assistance with XRD, to Dr. Alan Burton for technical support, and to Steve Hind-marsh for STEM specimen preparation. We thank Professor Chris Weber for valuable discussions.

Notes and references

1 A. Laha, S. Yoshida, F. M. dos Santos Vieira, H. Yi, S. H. Lee, S. V. G. Ayyagari, Y. Guan, L. Min, J. G. Jimenez, L. Miao, D. Graf, S. Sarker, W. Xie, N. Alem, V. Gopalan, C.-Z. Chang, I. Dabo and Z. Mao, *Nat. Commun.*, 2024, **15**, 3532.
2 M. Kondo, M. Ochi, T. Kojima, R. Kurihara, D. Sekine, M. Mat-subara, A. Miyake, M. Tokunaga, K. Kuroki, H. Murakawa, N. Hanasaki and H. Sakai, *Commun. Mater.*, 2021, **2**, 49.
3 M. A. Farhan, G. Lee and J. H. Shim, *J. Phys.: Condens. Matter*, 2014, **26**, 042201.
4 C. P. Weber, M. G. Masten, T. C. Ogloza, B. S. Berggren, M. K. Man, K. M. Dani, J. Liu, Z. Mao, D. D. Klug and A. A. Adeleke, *et al.*, *Phys. Rev. B*, 2018, **98**, 155115.
5 S. Ramankutty, *et al.*, *SciPost Phys.*, 2018, **4**, 010.
6 H. J. Park, L. J. Sandilands, J. S. You, H. S. Ji, C. H. Sohn, J. W. Han, S. J. Moon, K. W. Kim, J. H. Shim, J. S. Kim and T. W. Noh, *Phys. Rev. B*, 2016, **93**, 205122.
7 Y. Liu, T. Ma, L. Zhou, W. E. Straszheim, F. Islam, B. A. Jensen, W. Tian, T. Heitmann, R. A. Rosenberg, J. M. Wilde, B. Li, A. Kreyssig, A. Goldman, I. B. G. Ueland, R. J. McQueeney and D. Vaknin, *Phys. Rev. B*, 2019, **99**, 054435.
8 J. S. You, I. Lee, E. Choi, Y. Jo, J. Shim and J. S. Kim, *Curr. Appl. Phys.*, 2019, **19**, 230–235.
9 A. Saadi, L. Omari, A. Lekdadri, H. Lassri and A. Boudali, *Mater. Today: Proc.*, 2021, **37**, 3821–3826.
10 B. Liu, Y. Fu, J. Cheng, W. Zhu, J. He, C. Liu, L. Li and Y. Luo, *J. Supercond. Novel Magn.*, 2022, **35**, 3263–3269.
11 C. P. Weber, *J. Appl. Phys.*, 2021, **129**, 070901.
12 K. Takahashi, J. Shiogai, H. Inoue, S. Ito, S. Kimura, S. Awaji and A. Tsukazaki, *AIP Adv.*, 2020, **10**, 105216.
13 X. Yan, C. Zhang, S.-S. Liu, Y.-W. Liu, D. W. Zhang, F.-X. Xiu and P. Zhou, *Front. Phys.*, 2017, **12**, 127209.
14 C. W. Burrows, A. Dobbie, M. Myronov, T. P. Hase, S. B. Wilkins, M. Walker, J. J. Mudd, I. Maskery, M. R. Lees and C. F. McConville, *et al.*, *Cryst. Growth Des.*, 2013, **13**, 4923–4929.
15 W. Braun, A. Trampert, V. M. Kaganer, B. Jenichen, D. K. Satapathy and K. H. Ploog, *J. Cryst. Growth*, 2007, **301–302**, 50–53.
16 C. W. Burrows, T. P. Hase and G. R. Bell, *Phys. Status Solidi A*, 2019, **216**, 1800600.
17 C. W. Burrows, A. Dobbie, M. Myronov, T. P. A. Hase, S. B. Wilkins, M. Walker, J. J. Mudd, I. Maskery, M. R. Lees, C. F. McConville, D. R. Leadley and G. R. Bell, *Cryst. Growth Des.*, 2013, **13**, 4923–4929.
18 M. F. Kabir, M. T. Islam, S. Komatsu and M. Akabori, *Jpn. J. Appl. Phys.*, 2023, **63**, 01SP37.
19 C. Burrows, J. Aldous and G. Bell, *Results Phys.*, 2019, **12**, 1783–1785.
20 J. D. Aldous, C. W. Burrows, I. Maskery, M. Brewer, D. Pickup, M. Walker, J. Mudd, T. P. Hase, J. A. Duffy, S. Wilkins, C. Sánchez-Hanke and G. R. Bell, *J. Cryst. Growth*, 2012, **357**, 1–8.
21 G. R. Bell, *Molecular Beam Epitaxy*, Elsevier, 2nd edn, 2018, pp. 1–25.
22 W. Braun, A. Trampert, V. M. Kaganer, B. Jenichen, D. K. Satapathy and K. H. Ploog, *J. Cryst. Growth*, 2007, **301302**, 50–53.
23 S. Hatfield and G. Bell, *J. Cryst. Growth*, 2006, **296**, 165–173.
24 N. Nateghi, D. Ménard and R. A. Masut, *J. Appl. Phys.*, 2014, **116**, 133512.
25 K. Momma and F. Izumi, *J. Appl. Crystallogr.*, 2011, **44**, 1272–1276.
26 W. Tremel and R. Hoffmann, *J. Am. Chem. Soc.*, 1987, **109**, 124–140.
27 J. Park, G. Lee, F. Wolff-Fabris, Y. Koh, M. Eom, Y. K. Kim, M. Farhan, Y. Jo, C. Kim and J. Shim, *et al.*, *Phys. Rev. Lett.*, 2011, **107**, 126402.
28 G. A. Papoian and R. Hoffmann, *Angew. Chem., Int. Ed.*, 2000, **39**, 2408–2448.
29 R. People and J. C. Bean, *Appl. Phys. Lett.*, 1985, **47**, 322–324.
30 A. Braun, K. Briggs and P. Böni, *J. Cryst. Growth*, 2002, **241**, 231–234.
31 A. Jain, S. P. Ong, G. Hautier, W. Chen, W. D. Richards, S. Dacek, S. Cholia, D. Gunter, D. Skinner and G. Ceder, *et al.*, *APL Mater.*, 2013, **1**, 011002.
32 J. D. Aldous, C. W. Burrows, A. M. Sánchez, R. Beanland, I. Maskery, M. K. Bradley, M. dos Santos Dias, J. B. Staunton and G. R. Bell, *Phys. Rev. B: Condens. Matter Mater. Phys.*, 2012, **85**, 060403.
33 X. R. Huang, J. Bai, M. Dudley, B. Wagner, R. F. Davis and Y. Zhu, *Phys. Rev. Lett.*, 2005, **95**, 086101.
34 M. H. Xie, L. X. Zheng, S. H. Cheung, Y. F. Ng, H. Wu, S. Y. Tong and N. Ohtani, *Appl. Phys. Lett.*, 2000, **77**, 1105–1107.

View Article Online

35 S. Chen, Z. Chen, W. Chen, P. Fang, J. Liang, X. Wang, G. Wang and Y. Pei, *J. Alloys Compd.*, 2024, **989**, 174388.
36 E. Zallo, S. Cecchi, J. E. Boschker, A. M. Mio, F. Arciprete, S. Privitera and R. Calarco, *Sci. Rep.*, 2017, **7**, 1466.
37 G. Bell, C. McConville and T. Jones, *Appl. Surf. Sci.*, 1996, **104–105**, 17–23.
38 R. Magri and A. Zunger, *Phys. E*, 2002, **13**, 325–328.
39 J. Steinshnider, M. Weimer, R. Kaspi and G. W. Turner, *Phys. Rev. Lett.*, 2000, **85**, 2953–2956.
40 X. Li, Y. Zhang, D. Jiang, F. Guo, D. Wang and L. Zhao, *Superlattices Microstruct.*, 2017, **104**, 390–396.
41 T. Henksmeier, P. Mahler, A. Wolff, D. Deutsch, M. Voigt, L. Ruhm, A. M. Sanchez, D. J. As, G. Grundmeier and D. Reuter, *Commun. Mater.*, 2024, **5**, 276.

Open Access Article. Published on 17 October 2025. Downloaded on 10/27/2025 9:57:55 PM.
This article is licensed under a Creative Commons Attribution 3.0 Unported Licence.

© 2025 The Author(s). Published by the Royal Society of Chemistry